PERGAMON

International Journal of Heat and Mass Transfer 44 (2001) 1127–1141

International Journal of HEAT and MASS TRANSFER

www.elsevier.com/locate/ijhmt

Comparison between laminar and turbulent heat transfer in a stationary square duct with transverse or angled rib turbulators

Akira Murata [a,*], Sadanari Mochizuki [b]

[a] *Graduate School of Bio-Applications and Systems Engineering, Tokyo University of Agriculture and Technology, 2-24-16 Nakacho, Koganei, Tokyo 184-8588, Japan*

[b] *Department of Mechanical Systems Engineering, College of Engineering, Tokyo University of Agriculture and Technology, 2-24-16 Nakacho, Koganei, Tokyo 184-8588, Japan*

Received 10 December 1999; received in revised form 11 May 2000

Abstract

Heat transfer in a rib-roughened duct was numerically simulated by using the second-order finite difference method in coordinates fitted to transverse or angled ribs. Turbulent and laminar cases of which Reynolds numbers were 350 and 50, respectively, were computed for rib angles of 60° and 90°. The present turbulent results clearly showed the locally high heat transfer spots at several locations. The comparison between the laminar and turbulent results showed clear differences in heat transfer distribution because the higher momentum fluid of the turbulent case was more disturbed by the ribs as compared to the laminar case.

1. Introduction

In the development of high performance gas turbines, effective blade cooling is essential because the higher efficiency of the turbine requires a higher inlet gas temperature. Generally, this blade cooling is performed by film cooling at the external surface of the turbine blade and also by internal forced-convection cooling which uses winding flow passages inside the turbine blade. The film cooling is an effective cooling method, but it lowers the fluid dynamic efficiency of the blade and the thermal efficiency of the thermodynamic cycle by ejecting air to the blade surface and consequently by lowering the gas temperature. Therefore, the further advancement of the internal forced-convection cooling is needed. In internal forced-convection cooling, the real phenomena are very complicated due to external forces: the Coriolis force and the buoyancy force in the centrifugal acceleration field. In addition to these external forces, the effects induced by a 180° sharp turn and turbulence promoters (ribs) installed on the opposing internal surfaces result in phenomena that are far from understood [1].

As for the local heat transfer of a rib-roughened duct, several researchers investigated the spatial variation of the local heat transfer with various techniques: wall temperature measurement by using thermocouples [2–4], naphthalene sublimation technique [5,6], and wall temperature measurement by using temperature-sensitive liquid crystal [7–9]. In these studies, the heat transfer variation induced by the flow separation and reattachment behind the rib was captured to a certain extent. However, it is difficult to perform experiments in a rotating condition which can identify the flow structure and its influence on the heat transfer. Thus, further progress in experimental studies has so far been prevented.

In previous numerical studies of rib-roughened ducts, the Reynolds-averaged Navier–Stokes equation with a turbulence model was solved for transverse [10] and angled [11,12] rib configurations. Launder et al. [13] pointed out that in order to quantitatively simulate the flow in a rotating system, the second moment closure, that is, the Reynolds stress equation model, is a minimum requirement considering a non-isotropic effect of the Coriolis force on turbulence. Although this approach

* Corresponding author. Tel.: +81-42-388-7089; fax: +81-42-385-7204.

E-mail address: murata@mmlab.mech.tuat.ac.jp (A. Murata).

0017-9310/01/$ - see front matter
PII: S0017-9310(00)00180-0

Nomenclature

c_p	specific heat (J/(kg K))
C_S	Smagorinsky constant
D	side length of square duct (= hydraulic diameter) (m)
e	side length of ribs (m)
F_i	external force term ($(F_1, F_2, F_3) = (0, 0, 2)$)
h	heat transfer coefficient (W/(m^2 K))
J	Jacobian of coordinate transformation
l	length scale ($= 0.5D$) (m)
L_p	peripheral location (origin is at $(x, y) = (-1, +1)$)
Nu	Nusselt number ($= h\,D/\lambda$)
p	dimensionless pressure
P	rib pitch ($= D$) (m)
Pr	Prandtl number ($= 0.71$)
Pr_{SGS}	Prandtl number of subgrid-scale model ($= 0.5$)
$\dot{q}$	wall heat flux (W/m^2)
Re_m	Reynolds number ($= U_m D/\nu$)
Re_*	turbulent Reynolds number ($= u_* l/\nu$)
S_{ij}	rate-of-strain tensor
t	dimensionless time
T	temperature (K)
T_b	bulk temperature (K)
T_r	friction temperature ($= \dot{q}/(\rho c_p u_*)$) (K)
u, v, w	dimensionless velocities in x, y, z directions
u_*	mean friction velocity (m/s)
U^j	dimensionless contravariant velocity
U_m	mean velocity (m/s)
x, y, z	transverse, vertical, streamwise directions
$\Delta x, \Delta y, \Delta z$	grid spacing in x, y, z directions
$\alpha_{SGS\,j}$	subgrid-scale energy flux
γ	rib angle (°)
λ	thermal conductivity (W/(m K))
ν	kinematic viscosity (m^2/s)
ν_{SGS}	dimensionless subgrid-scale eddy viscosity
ρ	density (kg/m^3)
θ	dimensionless temperature ($= (T - T_b)/T_r$)
$\tau_{SGS\,ij}$	subgrid-scale stress tensor
τ_w	streamwise component of wall shear stress (Pa)
ξ, η, ζ	curvilinear coordinates

Subscripts and superscripts

L	local value
m	duct average or based on mean velocity
w	wall
∞	fully developed
*	friction velocity or defined by using u_*
+	dimensionless value based on inner scales
−	grid resolvable component

using the Reynolds-averaged turbulence model could reproduce the heat transfer of blade cooling to a certain extent, even the Reynolds stress equation model has empirical constants and functions which have to be adjusted depending on the flow field, and therefore the applicability of the model should carefully be examined. Recent advancement in computers enables us to numerically simulate the fluctuating components of the turbulent flow by using the large eddy simulation (LES) or the direct numerical simulation (DNS). Because LES and DNS directly resolve temporal variation of the fluctuating components, the results are more universal, in other words, more free from the empirical modeling than the Reynolds-averaged turbulence models. So far, the turbulent flow in a stationary smooth duct with a square cross section was solved using DNS [14,15] and LES [16,17].

The authors' group has performed heat transfer measurements by using thermocouples in both stationary and rotating conditions [2–4]. Recently, numerical analyses were also performed by using a dynamic subgrid-scale model for a rotating smooth duct of which cross section was square [18] and rectangular [19], and the technique was further applied to a rotating transversely rib-roughened duct [20,21]. In our previous numerical results, the followings were examined and clarified: the effect of duct cross-sectional aspect ratio on the Coriolis induced secondary flow, the dissimilarity between the velocity and temperature fields induced by the flow separation and reattachment, and the very high heat transfer area located in front of the ribs which was caused by the unsteady movement of the separation bubbles there. However, because of the Cartesian coordinate limitation, only the transverse rib case was treated in the previous studies, and therefore the effect of the secondary flow induced by angled ribs on the heat transfer has not been investigated yet.

This study examines the effect of the angled rib on the flow and heat transfer by performing the LES. In order to focus on the effects of the flow separation and reattachment caused by the ribs and the secondary flow induced by the angled ribs on the heat transfer, only the stationary conditions are computed in this study. These effects are examined by making a comparison between the laminar and turbulent cases and also between angled 60° and transverse 90° [21] rib cases.

2. Numerical analysis

Fig. 1 shows the computational domain and coordinate system used in this study. The duct had a square cross section with a side length of D which is the hydraulic diameter. The coordinate system was fixed to the duct, and the streamwise (radially outward) direction was chosen in the z direction; the x and y directions were transverse and perpendicular directions to the rib-roughened walls, respectively. In this study, two rib-roughened walls were distinguished by using the value of y ($y = +1$ and -1). Ribs were installed with the rib angle, γ, and the case of $\gamma = 60°$ was computed in this study. By assuming the periodicity of the flow field with the streamwisely repeated ribs, streamwise one span was chosen for the computational domain. The cross section of the rib was square (side length of $0.1D$), and streamwise pitch was set equal to the hydraulic diameter, D. This rib arrangement gave the rib height-to-hydraulic diameter ratio of 0.1 and the rib pitch-to-rib height ratio of 10. This rib arrangement was chosen because it was within the previously reported optimal range [22,23]. The rib angle, 60°, was chosen as the angle which gave the maximum heat transfer in the study of Han et al. [24].

The present procedure of the numerical analysis was the extension of our previous procedure [18–21] to a generalized curvilinear coordinate system. After applying a filtering operation to the incompressible Navier–Stokes equation with a filter width equal to the grid spacing [16], the dimensionless governing equations scaled by a length scale, l ($= 0.5D$), and mean friction velocity, u_*, became a set of dimensionless governing equations with respect to grid resolvable components indicated by overbars as $(\bar{u}, \bar{v}, \bar{w})$ under the assumption of constant fluid properties. In order to simulate a fully developed situation, the pressure and temperature fields were decomposed into a steady component changing linearly in the streamwise direction and the remaining components [25]. When this decomposition was used, the latter components became periodic in the streamwise direction, and they were used as the pressure and the temperature in this study. The former component was treated as an additional term in the governing equation. An external force term, F_i, had the mean pressure gradient term with a value of two in the streamwise direction: $(F_1, F_2, F_3) = (0,\ 0,\ 2)$. This mean pressure gradient term came from the above-mentioned steady pressure component changing linearly in the streamwise direction. Because the mean pressure gradient which drove the flow in the streamwise direction was set to be constant in this study, the flow rate varied depending on the flow conditions (e.g. rib angle); therefore, the flow rate was not known a priori, and the flow rate was calculated from the resultant computed flow field after the fully developed condition was attained.

The temperature was made dimensionless by using a bulk temperature, T_b, and a friction temperature, T_r, as $\theta = (T - T_b)/T_r$. Accordingly, the dimensionless energy equation was derived for the grid resolvable component, $\bar{\theta}$. In order to adopt the coordinate system fitted to the angled ribs, the governing equations in the Cartesian coordinates (x, y, z) were transformed into the generalized curvilinear coordinates (ξ, η, ζ). Although a slanted grid system was enough for the present angled straight rib cases, the computer program can handle the fully generalized curvilinear coordinate system considering future extension of the subject. The governing equations in the curvilinear coordinate system were expressed as follows [26]:

$$\frac{1}{J}\frac{\partial J\bar{U}^j}{\partial \xi^j} = 0, \tag{1}$$

$$\frac{\partial \bar{u}_i}{\partial t} = -\bar{U}^j\frac{\partial \bar{u}_i}{\partial \xi^j} - \frac{\partial \xi^j}{\partial x_i}\frac{\partial \bar{p}}{\partial \xi^j} + \frac{1}{Re_*}\frac{\partial \xi^j}{\partial x_l}\frac{\partial}{\partial \xi^j}\left(\frac{\partial \xi^k}{\partial x_l}\frac{\partial \bar{u}_i}{\partial \xi^k}\right) + \frac{\partial \xi^k}{\partial x_j}\frac{\partial \tau_{\mathrm{SGS}\,ij}}{\partial \xi^k} + F_i, \tag{2}$$

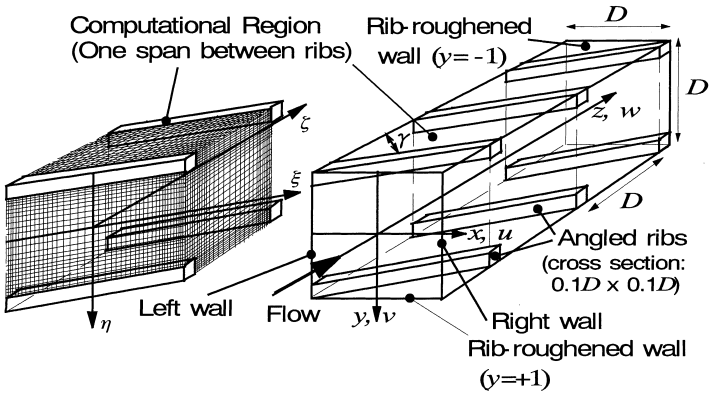

Fig. 1. Schematic of a rib-roughened duct and a coordinate system fitted to angled ribs.

$$\frac{\partial\bar{\theta}}{\partial t} = -\bar{U}^j \frac{\partial\bar{\theta}}{\partial\xi^j} - \frac{2\bar{w}}{\bar{w}_m} + \frac{1}{Re_* Pr} \frac{\partial\xi^j}{\partial x_l} \frac{\partial}{\partial\xi^j}\left(\frac{\partial\xi^k}{\partial x_l}\frac{\partial\bar{\theta}}{\partial\xi^k}\right) + \frac{\partial\xi^k}{\partial x_j}\frac{\partial\alpha_{\mathrm{SGS}\,j}}{\partial\xi^k}, \tag{3}$$

where $\bar{U}^j$ was a contravariant component of velocity, and the following expressions were assumed: $J = \partial(x,y,z)/\partial(\xi,\eta,\zeta)$, $(x_1,x_2,x_3) = (x,y,z)$, and $(\xi^1,\xi^2,\xi^3) = (\xi,\eta,\zeta)$.

Subgrid-scale components of stress, $\tau_{\mathrm{SGS}\,ij}$, and energy flux, $\alpha_{\mathrm{SGS}\,j}$, were expressed as follows:

$$\tau_{\mathrm{SGS}\,ij} = 2\nu_{\mathrm{SGS}}\bar{S}_{ij}, \tag{4}$$

$$\alpha_{\mathrm{SGS}\,j} = \frac{\nu_{\mathrm{SGS}}}{Pr_{\mathrm{SGS}}}\frac{\partial\xi^k}{\partial x_j}\frac{\partial\bar{\theta}}{\partial\xi^k}, \tag{5}$$

where

$$\bar{S}_{ij} = \frac{1}{2}\left(\frac{\partial\xi^k}{\partial x_j}\frac{\partial\bar{u}_i}{\partial\xi^k} + \frac{\partial\xi^k}{\partial x_i}\frac{\partial\bar{u}_j}{\partial\xi^k}\right), \tag{6}$$

$$\nu_{\mathrm{SGS}} = C_S^2(\Delta x\Delta y\Delta z)^{2/3}\sqrt{2\bar{S}_{ij}\bar{S}_{ij}}. \tag{7}$$

In our previous studies [18–21], the dynamic subgrid-scale model developed by Germano et al. [27] was used in order to calculate the value of C_S as a function of spatial location with the stable computational procedure of Lilly [28]; C_S was averaged taking advantage of the symmetric property in the transverse direction in addition to the time averaging in order to exclude negative values of C_S. However, the angled rib case of this study does not have geometric symmetry in the transverse direction, and therefore we adopted the Lagrangian dynamic subgrid-scale model of Meneveau et al. [29] which averaged the value of C_S along the stream line for a certain distance. The turbulent Prandtl number for the subgrid-scale component, Pr_{SGS}, was set to 0.5 [30]. The width of the test filter was double the grid spacing and the space filter was accurate to fourth-order.

Discretization was performed by a finite difference method using the collocated grid system [26]. The spatial and temporal discretization schemes were similar to those of [15]: the second-order central differencing method and the Crank–Nicolson method for the viscous term, and the second-order differencing method satisfying the consistency and the conservative property of the finite difference method [26] and the second-order Adams–Bashforth method for the convective term. The pressure field was treated following the MAC method [31], and the algebraic equation for each variable was solved by using the SOR method. The computational domain was one span between streamwise consecutive ribs (see Fig. 1), and the domain had the side length of 2, 2, and 2 in x, y, and z directions, respectively. This length, 2, can be expressed by using an inner length scale, ν/u_*, as 700 for the turbulent case.

The Reynolds numbers, Re_* $(= u_* l/\nu)$, were 50 and 350 for the laminar and turbulent cases, respectively. Table 1 summarizes the conversion of Re_* defined by using the friction velocity to Re_{m} defined by using the mean velocity. As explained above, the value of Re_{m} was calculated from the computed result; Re_{m} was not known a priori. At the wall boundary, no-slip and constant heat flux conditions were imposed, although the front and rear surfaces of the ribs were set to be adiabatic. This adiabatic condition was adopted to preserve the linear increase of the bulk temperature and also to consider the previous experiments in which the ribs were not heated. An additional computation with the constant heat flux condition at the front and rear surfaces of the ribs was also performed, and it was found that even when the front and rear surfaces of the ribs were heated, the conclusions of this study were not changed. At the inlet and outlet boundaries, the periodic boundary condition [25] was imposed in order to obtain a fully developed flow. The boundary conditions of the intermediate velocities and the pressure were set in the same procedure as that of [32,33].

The grids in the physical domain were contracted and became dense near the walls and the rib surfaces by using a tangent hyperbolic function (see Fig. 1). The grid number was $47 \times 47 \times 47$, and this grid configuration gave a grid spacing of $\Delta x^+ = 1.0$–38, $\Delta y^+ = 0.6$–52, and $\Delta z^+ = 3.6$–28 for the turbulent case of $Re_* = 350$. The effect of the grid spacing on the computed result was checked by increasing the grid number to $65 \times 65 \times 65$ for several cases, and no major difference was observed. The verification of the present computational procedure was also performed for the smooth straight duct as performed in [18], and the agreement with the previous DNS results [14,15] for the straight smooth square duct in the stationary condition was almost the same as that seen in [18]: the comparison was made in the mean velocity profile, the three components of the turbulence intensities, and the secondary flow intensity of the Prandtl's second kind. The time step interval was $\Delta t = 1.0 \times 10^{-4}$, which can be expressed as $\Delta t^+ = 0.035$ for $Re_* = 350$ when made dimensionless by an inner time scale, ν/u_*^2. The computation was started using the result of the similar condition as an initial condition. The calculations were carried out to 120,000 steps to

Table 1
Conversion of the Reynolds number, Re_*, into the conventional form, Re_{m}, by using the computed flow rate

	γ			
	90°		60°	
Re_*	50	350	50	350
Re_{m}	1034	4106	480	3148

fully develop the flow. After the initial 120,000 steps were performed, additional 400,000 steps ($t=40$ or $t^+=14{,}000$ for $Re_*=350$) were performed for computing the statistical values of turbulent flow. This 400,000 step computation needed about 76 CPU hours using an NEC SX4B. In the laminar cases, the solution of the steady state at 80,000 steps was used. In this study, the second order scheme was used because of its lighter computational load in order to obtain statistically steady results by increasing the total time steps. The influence of the order of the scheme was discussed in detail in [21], and it was verified that the difference between the second and forth order schemes did not change the results.

3. Results and discussion

3.1. Comparison between laminar and turbulent flow fields

Fig. 2 shows the velocity vectors of the 90° rib case in the y–z plane at two transverse locations. In the figure, the time-averaged vectors for turbulent flow ($Re_*=350$, left figures) and the vectors at the steady state for laminar flow ($Re_*=50$, right figures) are shown. In both cases, the flow passing beyond the ribs is seen. In the turbulent case, the flow separation behind the ribs and its reattachment which are symmetric with respect to the horizontal plane of $y=0$ are observed, although in the laminar case a clear flow reattachment between the ribs is not observed; this point will be explained in detail later by showing the velocity vectors in the x–z plane and the wall shear stress. Fig. 3 shows the results of the 60° rib case. In the figure, the horizontal axis denotes the streamwise location adjusted to fit between 0 and 2 by subtracting the streamwise location of the angled rib (0.06, 0.58, and 1.09) at each transverse location. In the 60° rib case, the flows near the left and right walls become different from each other due to the secondary flow induced by the angled rib. When the turbulent and laminar results are compared, they can be seen to have the following similar characteristics: near the left wall (Fig. 3(a)) the flows beyond the ribs and directing to the rib-roughened wall to reattach are intense, and near the right wall (Fig. 3(c)) these flows become weaker. In addition, near the right wall, the flow directing to the

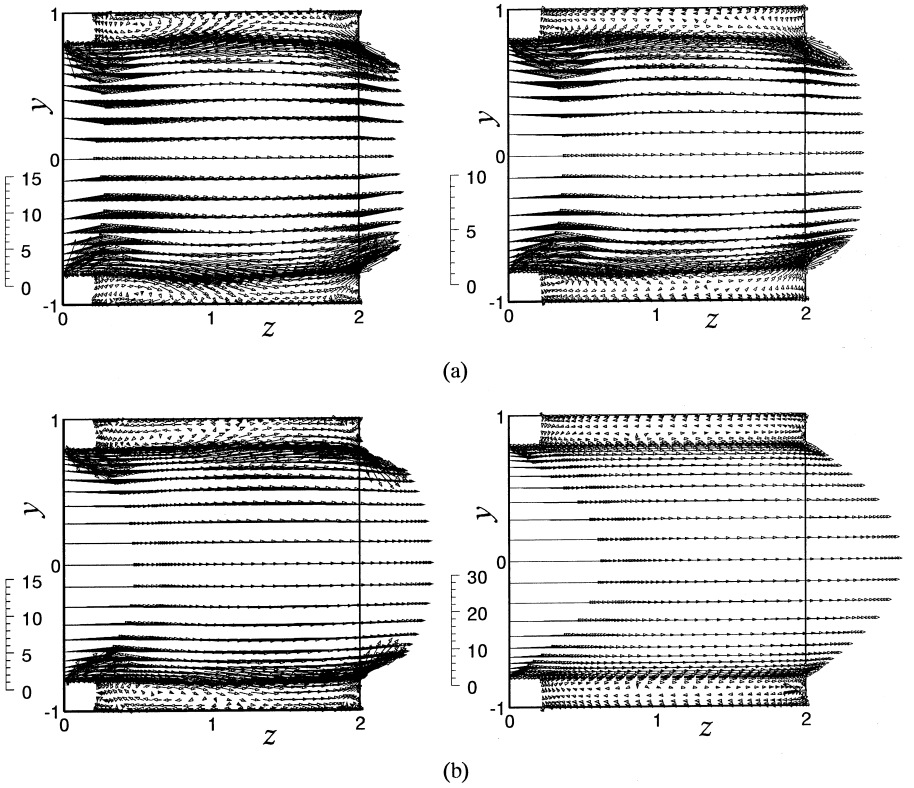

Fig. 2. Velocity vectors in y–z plane (90° rib; left and right figures are for turbulent flow ($Re_*=350$) and laminar flow ($Re_*=50$), respectively. For turbulent and laminar flows, the time-averaged and steady-state vectors are shown, respectively. The scale in each figure indicates the vector magnitude). (a) Near left wall ($x=-0.9$). (b) At transverse center ($x=0$).

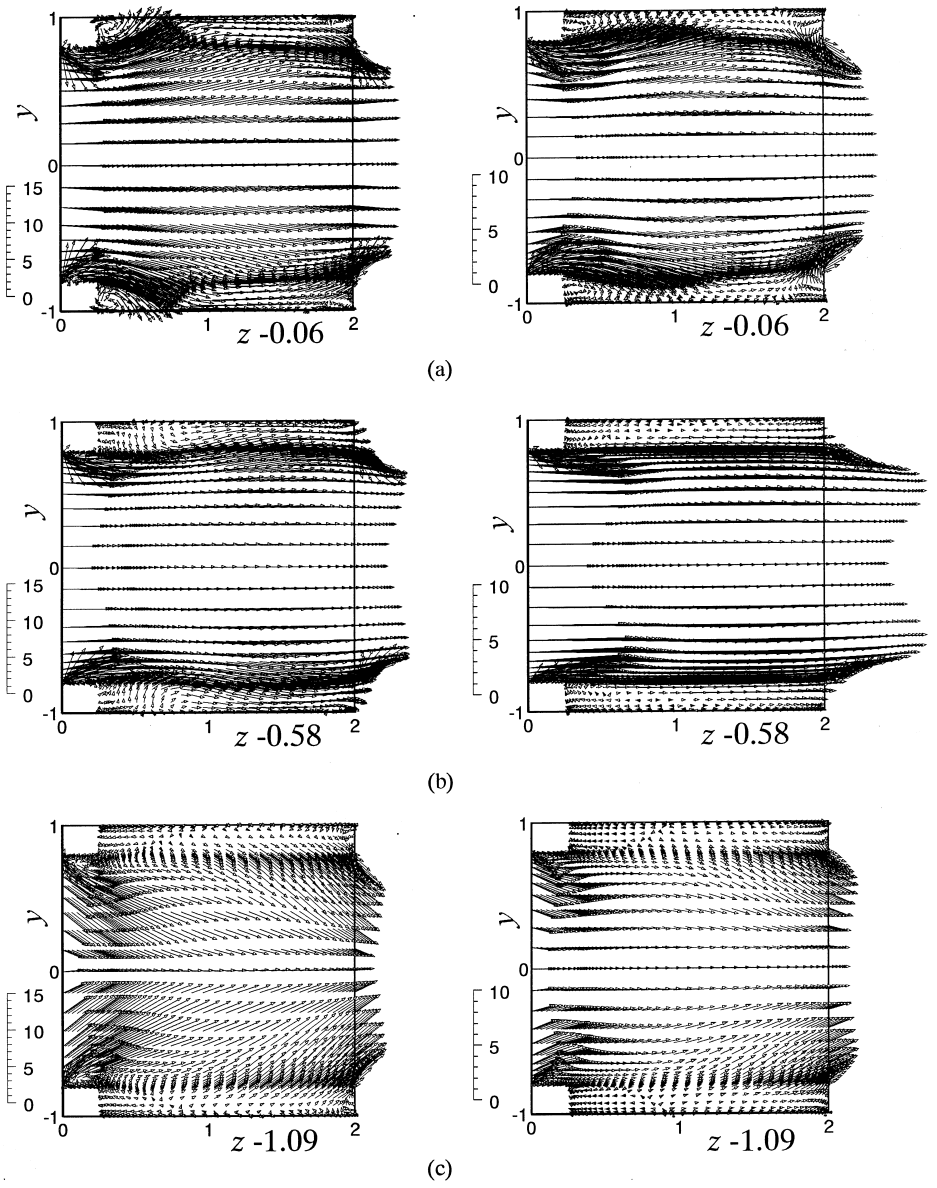

Fig. 3. Velocity vectors in y–z plane at three different transverse locations (60° rib; legend is the same as that of Fig. 2): (a) near left wall ($x = -0.9$); (b) at transverse center ($x = 0$); (c) near right wall ($x = +0.9$).

horizontal symmetric plane ($y = 0$) dominates because the flow directing along the angled ribs changes its direction to $y = 0$ due to the existence of the right wall.

Fig. 4 shows the velocity vectors of the 90° rib case in the x–y planes at the following three different streamwise locations: (a) at the rib location (rib streamwise center); (b) at the midpoint between the consecutive ribs; and (c) in front of the ribs (a half of rib width from the ribs). At first, the turbulent case (left figures) is explained. At the rib location (Fig. 4(a) left), the vertical velocity component leaving from the rib is clearly seen. Near the smooth side walls, the existence of the rib induces the flow going from the rib-roughened wall to the horizontal symmetric plane ($y = 0$) as previously observed in the experiments [7,34]. In the plane between the ribs (Fig. 4(b) left), the flow directing to the rib-roughened (upper and lower) walls is seen. This flow composes the reattachment of the separated flow occurring around the midpoint between ribs. The flow then changes its direction to the side walls, although the flow directing to the opposite direction (to the transverse center) is also seen in the region very close to the rib-roughened wall

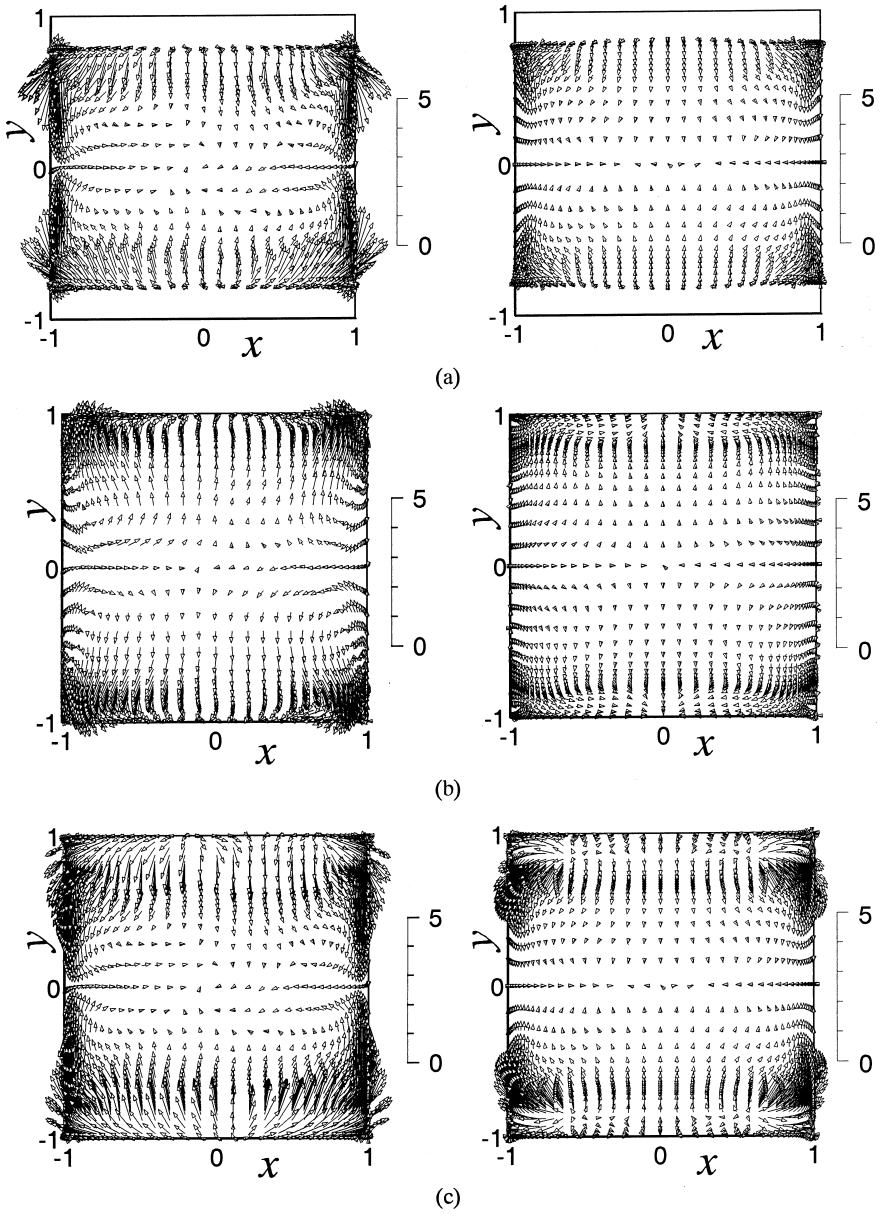

Fig. 4. Velocity vectors in x–y plane at three different streamwise locations (90° rib; legend is the same as that of Fig. 2): (a) at rib location (at center in rib width); (b) at midpoint between ribs; (c) in front of ribs (a half of rib width from ribs).

[21]. In the laminar case (Fig. 4(b) right), the flow directing to the transverse center is seen in the thicker area near the rib-roughened wall than that in the turbulent case. In front of the ribs (Fig. 4(c)) of both turbulent and laminar cases, the flow component directing to the horizontal symmetric plane ($y = 0$) is formed because the flow has to go beyond the ribs. This flow leaving the ribs also has the velocity component directing to the side walls, and the velocity vector becomes larger in its magnitude closer to the side walls.

Fig. 5 shows the velocity vectors $(\overline{u}, \overline{v})$ in the ξ–η plane which is parallel to the 60° ribs. In the figure, the value in the ξ–η plane is projected onto the x–y plane. In the 60° rib case, the following characteristics are common in the turbulent and laminar cases, although the magnitude of the secondary flow differs. At the rib location (Fig. 5(a)), the flow components passing beyond the ribs and along the angled ribs from left to right in the figure are seen except the region close to the left wall (left-hand side wall in the figure). The flow along the ribs

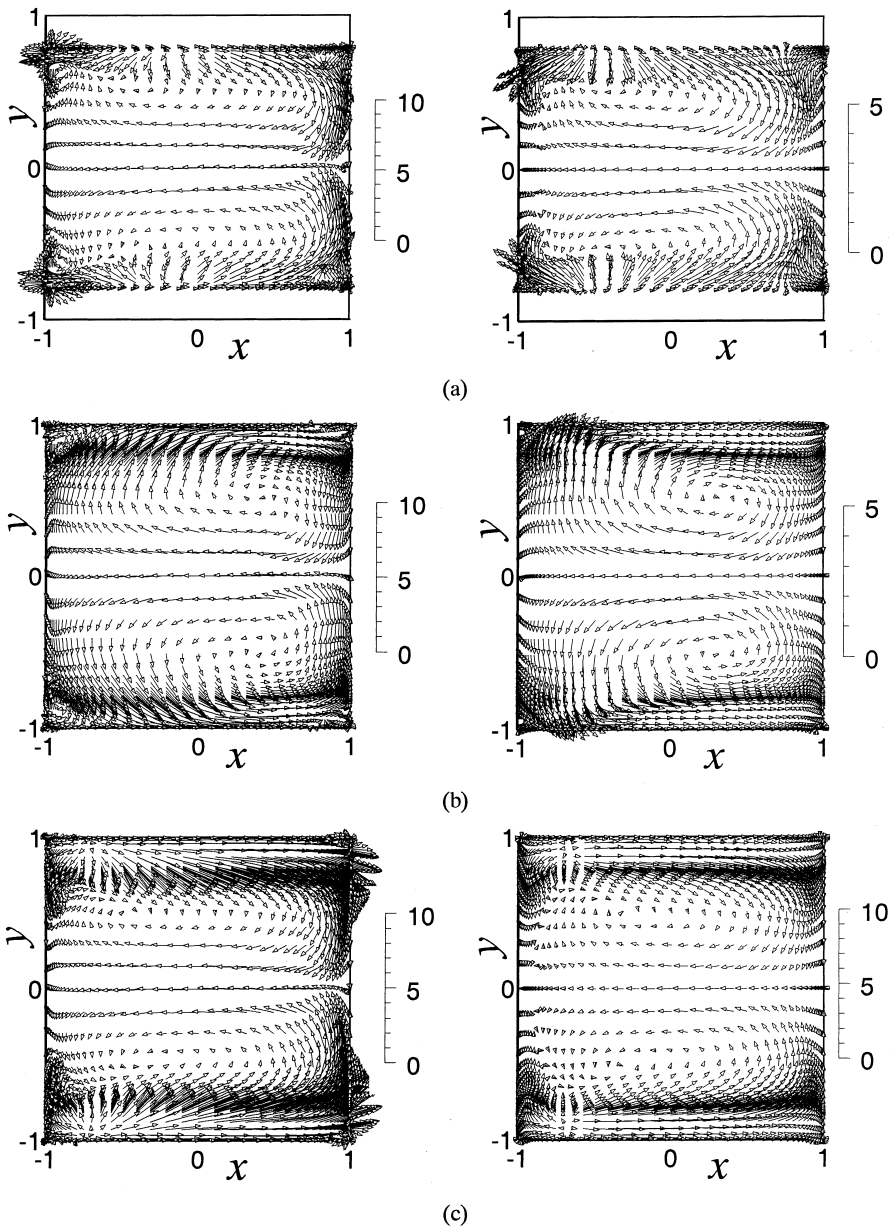

Fig. 5. Velocity vectors in ξ–η plane at three different streamwise locations (60° rib; figures are projected onto x–y plane; legend is the same as that of Fig. 2): (a) at rib location (at center in rib width); (b) at midpoint between ribs; (c) in front of ribs (a half of rib width from ribs).

changes its direction to the horizontal symmetric plane ($y=0$) near the right wall (right-hand side wall in the figure). This flow returns to the left wall at the horizontal symmetric plane ($y=0$), and it composes a pair of vortex. This pair of vortex also dominates the secondary flow in the other planes.

Fig. 6 shows the velocity vectors in the x–y plane which is parallel to the rib-roughened walls. The location of the plane is at a half of rib height from the rib-roughened wall at $y=-1$. In the laminar 90° rib case of Fig. 6(a) (right), as explained in Fig. 2, the central area of the rib-roughened surface is covered by the reverse flow from right to left in the figure, and the reattachment point cannot be seen. In the turbulent 90° rib case (Fig. 6(a) left), the reattachment point is seen at about $z=1$ where the velocity vectors become zero in their magnitude and change their direction from left to right. In the 60° rib case of Fig. 6(b), the flow component from

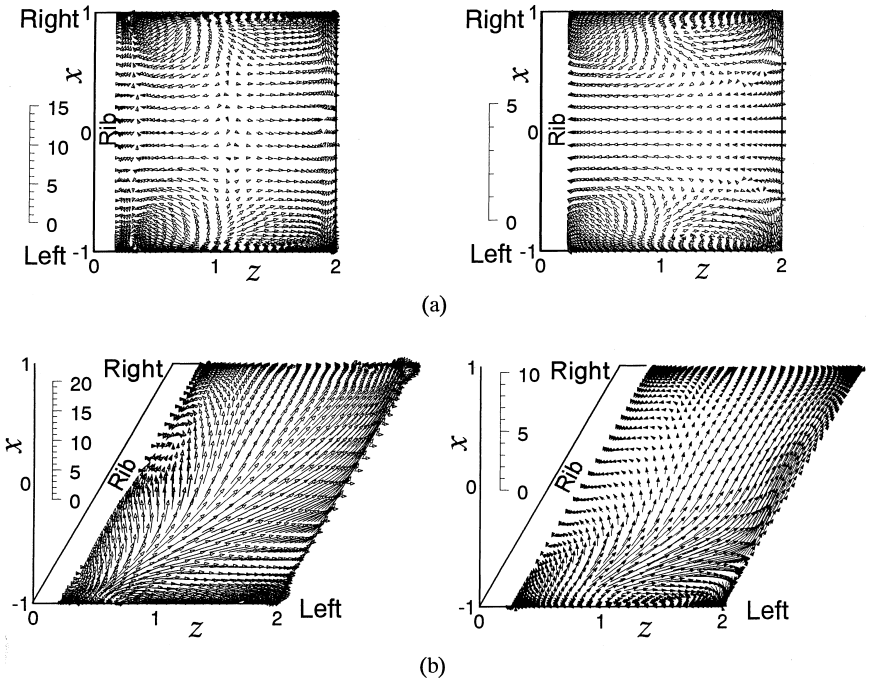

Fig. 6. Velocity vectors in x–z plane at a half of rib height from rib-roughened wall at $y=-1$ (legend is the same as that of Fig. 2): (a) 90° rib: near rib-roughened wall at $y=-1$; (b) 60° rib: near rib-roughened wall at $y=-1$.

the left wall to the right wall which is almost parallel to the angled ribs dominates, and the turbulent and laminar cases qualitatively agree with each other.

Fig. 7 shows the isocontours of the time-averaged streamwise velocity, $\overline{w}$, and temperature, $\overline{\theta}$, in the x–y planes at the same streamwise locations as in Fig. 4 for the turbulent 90° rib case. At the rib location (left figures), $\overline{w}$ and $\overline{\theta}$ are similar to each other, but at the midpoint between the ribs (middle figures), the density of the contour lines of $\overline{w}$ near the upper and lower rib-roughened walls become larger than that of $\overline{\theta}$. The similarity between the velocity and temperature fields is broken by the flow separation and reattachment induced by the ribs. In this study, the term, "dissimilarity" is used to describe the different profiles between $\overline{w}$ and $\overline{\theta}$ induced by the ribs. At the center of the side walls, the isocontour lines of $\overline{w}$ and $\overline{\theta}$ are projected to the duct center due to the secondary flow seen in Fig. 4. In the plane in front of the ribs (right figures), the profiles are almost similar to those at the midpoint between the ribs. The laminar 90° rib case of Fig. 8 also shows the slight dissimilarity between $\overline{w}$ and $\overline{\theta}$ near the upper and lower rib-roughened walls at the midpoint between the ribs and in front of the ribs. In the laminar case, the projected profile at the center of the side wall and the uniformity of $\overline{w}$ in the transverse direction are not seen, although both are observed in the turbulent case of Fig. 7. It can be said that the existence of the ribs does not affect the laminar flow field so much, because the fluid momentum of the laminar flow near the ribs is lower, and therefore the magnitude of the rib induced flow is smaller than the turbulent case.

Fig. 9 shows the isocontours of the time-averaged $\overline{w}$ and $\overline{\theta}$ in the ξ–η planes for the turbulent 60° rib case. Due to the secondary flow seen in Fig. 5, the profiles of both $\overline{w}$ and $\overline{\theta}$ have two peaks at the upper and lower locations shifted to the left wall. At the center of the right wall, the profile becomes projected to the duct center. As compared to the turbulent 90° rib case (Fig. 7), the similarity between $\overline{w}$ and $\overline{\theta}$ is more preserved, although at the midpoint between the ribs the density of the contour lines of $\overline{w}$ near the upper and lower rib-roughened walls becomes slightly larger than that of $\overline{\theta}$. In the laminar 60° rib case of Fig. 10, most of the characteristics are similar to those of the turbulent 60° rib case, and the dissimilarity between $\overline{w}$ and $\overline{\theta}$ is also observed at the midpoint between the ribs (middle figure) near the upper and lower rib-roughened walls.

3.2. Comparison in distribution of wall shear stress and Nusselt number

Fig. 11 shows the time-averaged values of the streamwise component of the wall shear stress (Fig. 11(a)) and the local Nusselt number (Fig. 11(b)) on the four walls for the turbulent 90° rib case. The Nusselt

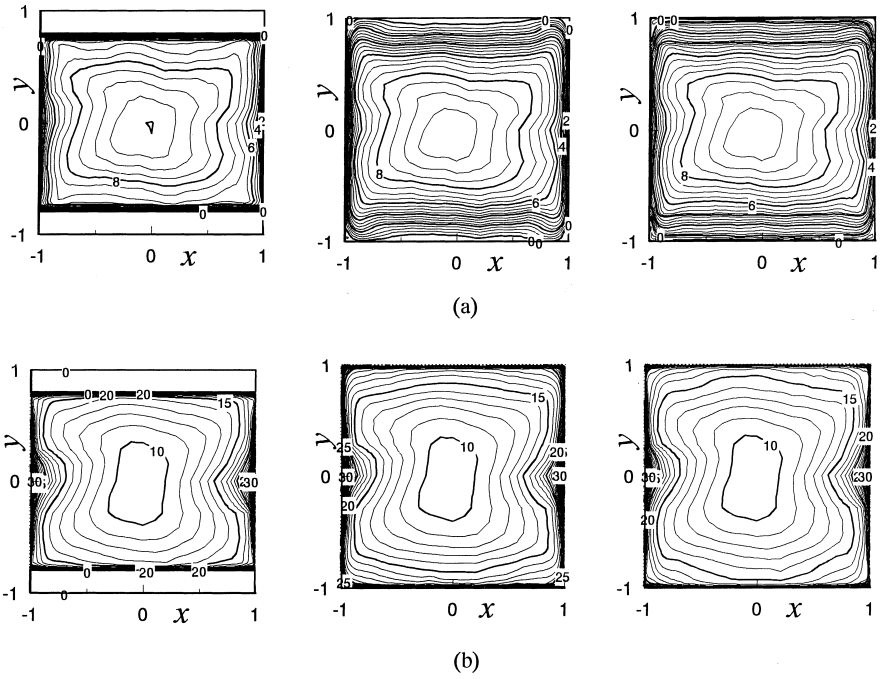

Fig. 7. Isocontours of time-averaged variables in x–y plane for turbulent flow (90° rib, $Re_* = 350$; left, middle, and right figures are for the planes at rib location, at midpoint between ribs, and in front ribs (a half of rib width from ribs), respectively): (a) streamwise velocity, $\overline{w}$; (b) temperature, $\overline{\theta}$.

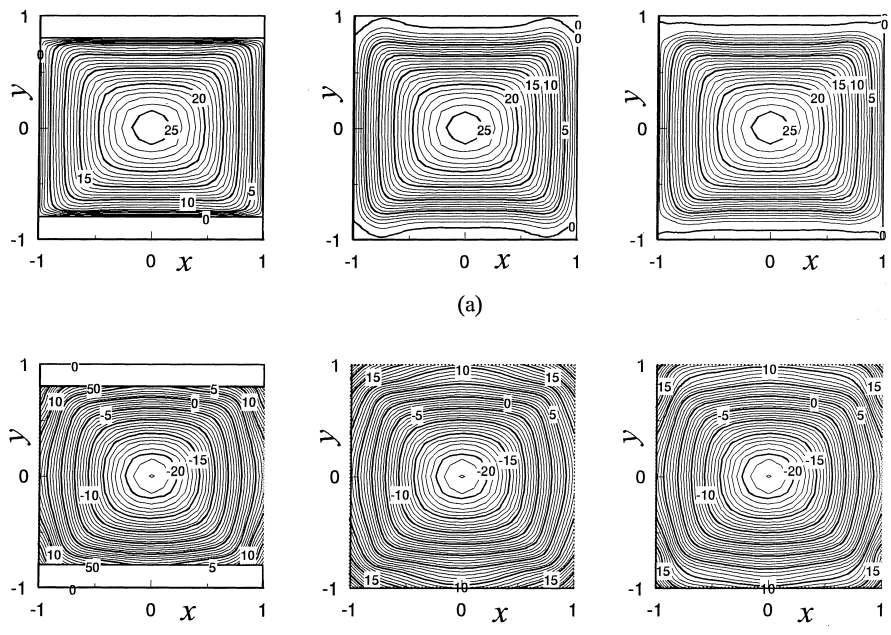

Fig. 8. Isocontours of variables in x–y plane for laminar flow (90° rib, $Re_* = 50$; legend is the same as that of Fig. 7): (a) streamwise velocity, $\overline{w}$; (b) temperature, $\overline{\theta}$.

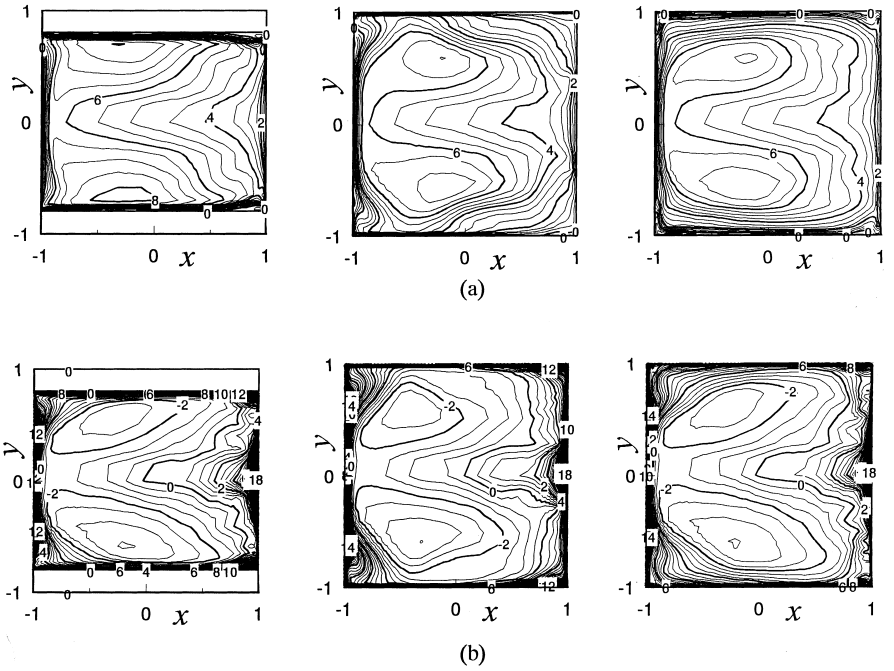

Fig. 9. Isocontours of time-averaged variables in ξ–η plane for turbulent flow (60° rib, $Re_* = 350$; figures are projected onto x–y plane. Legend is the same as that of Fig. 7): (a) streamwise velocity, $\overline{w}$; (b) temperature, $\overline{\theta}$.

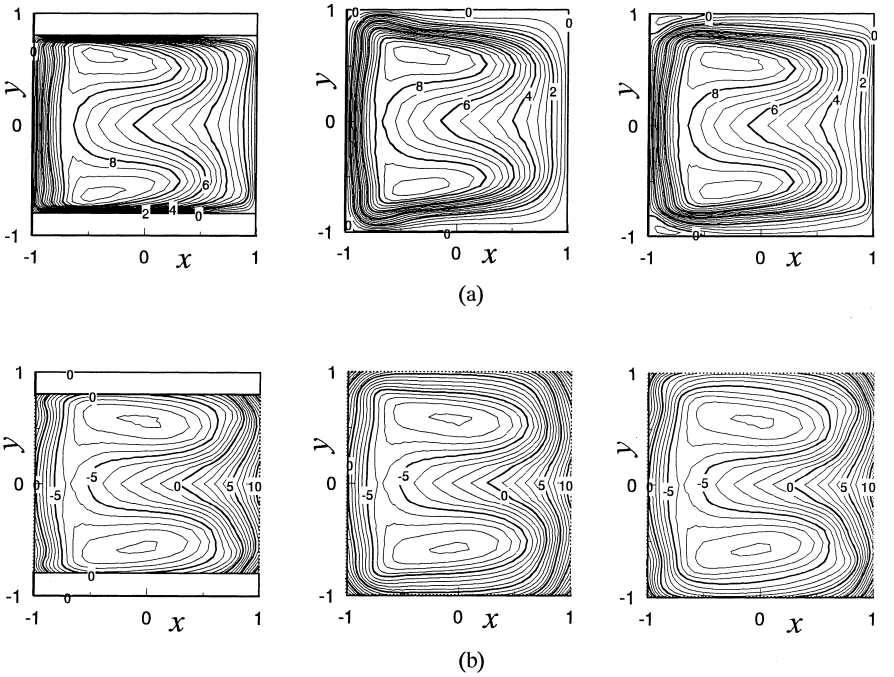

Fig. 10. Isocontours of variables in ξ–η plane for laminar flow (60° rib, $Re_* = 50$; figures are projected onto x–y plane. Legend is the same as that of Fig. 7): (a) streamwise velocity, $\overline{w}$; (b) temperature, $\overline{\theta}$.

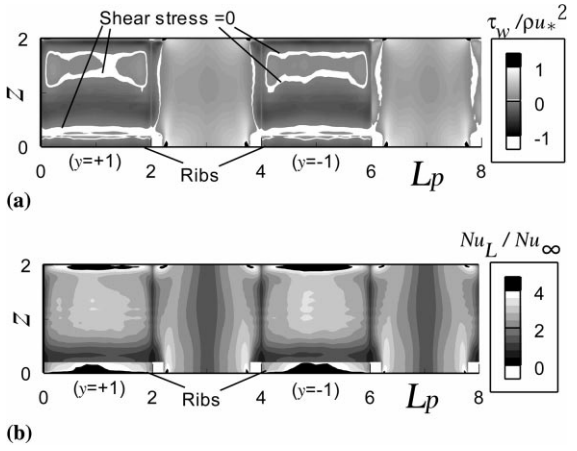

Fig. 11. Spatial variation of time-averaged streamwise wall shear stress and Nusselt number on four walls for turbulent flow (90° rib, $Re_* = 350$): (a) wall shear stress; (b) Nusselt number.

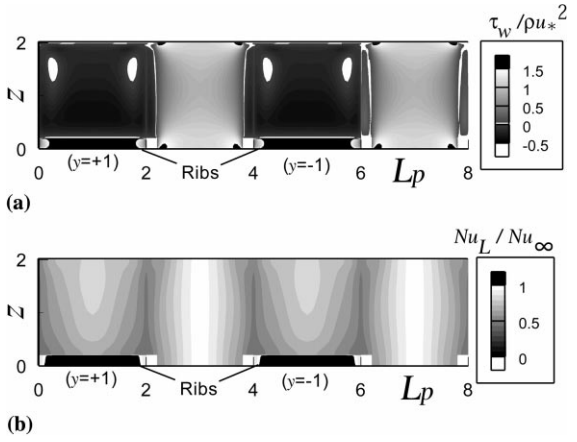

Fig. 12. Spatial variation of streamwise wall shear stress and Nusselt number on four walls for laminar flow at steady state (90° rib, $Re_* = 50$): (a) wall shear stress; (b) Nusselt number.

number was normalized using the following empirical correlation for a fully developed pipe flow [35]:

$$Nu_\infty = 0.022 Re_m^{0.8} Pr^{0.5}. \quad (8)$$

In the laminar case of Fig. 12, the Nusselt number was normalized using $Nu_\infty = 4.36$ [35]. In the figures, out-of-range values are shown by white and black solid areas for very low and very high values, respectively. In Figs. 11(a) and 12(a), 0 shear stress areas are also indicated by solid white. The horizontal axis of the figure denotes the peripheral location, L_p: $L_p = 0$, 2, 4, and 6 correspond to $(x, y) = (-1, +1), (+1, +1), (+1, -1)$, and $(-1, -1)$, respectively ($L_p = 0$ is identical to $L_p = 8$). As explained in our previous study [21], when the instantaneous values (not shown here) were compared, the locations where the absolute value of wall shear stress becomes large and small were highly correlated to the locations of high and low Nusselt numbers, respectively. The spots of large positive shear stress around the midpoint between the ribs corresponded to the sweep motion which transported cooler fluid from the main stream to the wall with high streamwise momentum. Therefore, the high heat transfer at the corresponding spots was reasonable. On the other hand, the spots of large negative shear stress were seen in front of the rib, and the spots also corresponded to the high heat transfer. This locally large negative shear stress was caused by the fluid which impinged on the wall in front of the rib after another impingement on the rib front surface. As a consequence, the high heat transfer areas are observed around the midpoint between the ribs and in front of the ribs in the time-averaged Nusselt number of Fig. 11(b). These high heat transfer areas were also observed in previous experimental results [6–9]. In the time-averaged shear stress of Fig. 11(a), only a flow separation bubble in front of the rib seems to exist, but it actually fluctuates and causes the high heat transfer by the unsteady effect of the low temperature and high momentum fluid.

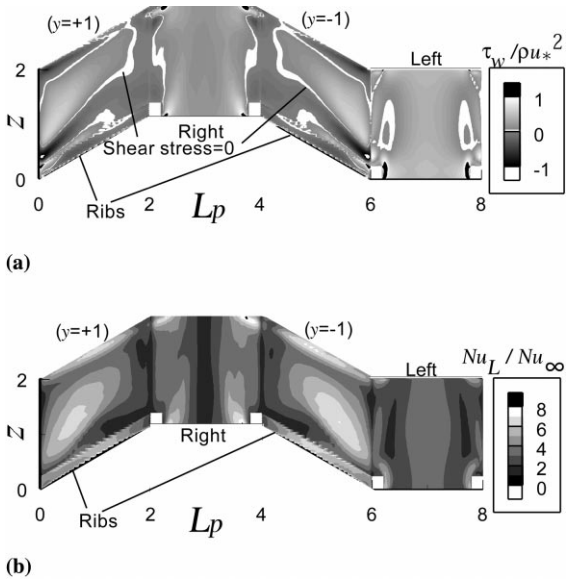

Fig. 13. Spatial variation of time-averaged streamwise wall shear stress and Nusselt number on four walls for turbulent flow (60° rib, $Re_* = 350$): (a) wall shear stress; (b) Nusselt number.

On the smooth side walls of Fig. 11, the area around the ribs shows the very high heat transfer which was also observed in the experiments [7,8] and can be understood by the high momentum fluid there. On the side walls, the wall-normal gradient at the central area is small because of the projected profile seen in Fig. 7, and therefore the

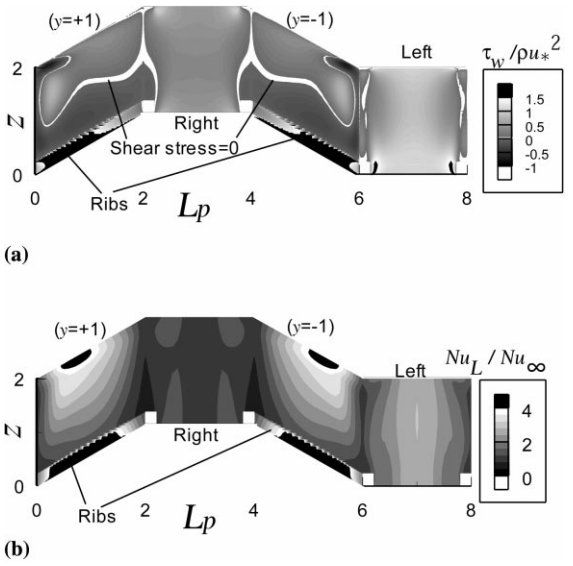

Fig. 14. Spatial variation of streamwise wall shear stress and Nusselt number on four walls for laminar flow at steady state (60° rib, $Re_* = 50$): (a) wall shear stress; (b) Nusselt number.

heat transfer is low there; on the other hand, the heat transfer around the ribs becomes very high, and at the area close to the rib-roughened walls, the heat transfer is also high.

In the laminar 90° rib case of Fig. 12, as discussed in Figs. 2 and 6, the wall shear stress becomes negative on the rib-roughened walls, and the reattachment does not occur. As compared to the turbulent flow, the laminar flow over a backward-facing step gives the longer reattachment distance [36], and therefore with the present rib configuration the reattachment is thought not to occur. The Nusselt number becomes higher around the central and downstream area between the ribs, although the very high heat transfer in front of the rib which was observed in the turbulent case does not exist, and the smooth side walls give the higher heat transfer than that on the rib-roughened wall.

The streamwise component of the wall shear stress and the Nusselt number are shown for the turbulent (Fig. 13) and laminar (Fig. 14) 60° rib cases. As seen in Fig. 6(b), the angled rib induces the inclined flow, and therefore it should be noted that the area surrounded by the zero streamwise wall shear stress does not necessarily correspond to the similar separation bubble as seen in the 90° rib case. In the figure, the notches around the ribs are caused by the inadequate interpolation ability of the software used in drawing the figure, and the numerical results themselves do not oscillate. In the Nusselt number distribution of the 60° rib case (Fig. 13(b)), the high heat transfer areas similar to the 90° rib case are observed at the midpoint between the ribs and in front of the ribs. The high heat transfer area at the midpoint between the ribs is shifted to the left wall, because near the left wall the flow reattachment is more intense than that near the right wall as seen in Fig. 3 (left). On the side walls (the right and left walls), the shear stress around the ribs is high, and at the same time the heat transfer is high there. At the central area of the right wall, the heat transfer becomes low because of the angled-rib induced secondary flow. In the laminar 60° rib case of Fig. 14, the negative wall shear stress in front of the ribs observed in the turbulent case disappears. The heat transfer on the rib-roughened wall gives a local maximum in front of the rib (Fig. 14(b)); however, this area has the positive wall shear stress, and therefore this is different from the high heat transfer area of the turbulent case which was correlated with the negative wall shear stress. In the laminar case, the high heat transfer area around the rib is not observed on the contrary to the turbulent case. It is common in both the turbulent and laminar cases that the central areas of the left and right walls give the high and low heat transfer, respectively, because of the angled-rib induced secondary flow.

As shown in Table 2, the present wall-averaged Nusselt number, Nu_w/Nu_∞, of the turbulent cases agreed with the experimental results of Chandra et al. [5] and Rau et al. [7]. However, it should be noted that the experimental condition differs from the computational condition, and the spatial resolution in the experiments of Chandra et al. [5] is low: three locations in the transverse direction.

4. Conclusions

In the turbulent cases of both 60° and 90° ribs, the flow reattachment at the midpoint between the ribs and

Table 2
Comparison between the present wall-averaged Nusselt number, Nu_w/Nu_∞, and the previous experimental results (the experimental result of Chandra et al. [5] is for $Re_m = 30{,}000$, $e/D = 0.063$, and $P/e = 10$; that of Rau et al. [7] is for $Re_m = 30{,}000$, $e/D = 0.1$, and $P/e = 10$)

	90° rib		60° rib		
	Ribbed wall	Side wall	Ribbed wall	Left wall	Right wall
Present results	2.2	2.0	3.4	2.8	3.0
Chandra et al. [5]	2.6	1.8	3.3	2.2	2.2
Rau et al. [7]	2.4	2.1	–	–	–

the unsteady reverse flow in front of the rib formed high values of the time-averaged heat transfer; especially the heat transfer in front of the rib became very high. However, in the laminar flow cases, the low momentum fluid near the rib-roughened wall resulted in the smaller effect of the rib on the flow field as compared to the turbulent case; the lack of the unsteady fluid motion also contributed to the different heat transfer profile of the laminar case from the turbulent case. Because of these smaller effects of the ribs in the laminar case, the dissimilarity between the velocity and temperature profiles was less than that in the turbulent case.

References

[1] B. Lakshminarayana, Fluid Dynamics and Heat Transfer of Turbomachinery, Wiley, New York, 1996, pp. 597–721 (Chapter 7).

[2] S. Mochizuki, A. Murata, M. Fukunaga, Effects of rib arrangements on pressure drop and heat transfer in a rib-roughened channel with a sharp 180° turn, Trans. ASME, J. Turbomachinery 119 (1997) 610–616.

[3] S. Mochizuki, M. Beier, A. Murata, T. Okamura, Y. Hashidate, Detailed measurement of convective heat transfer in rotating two-pass rib-roughened coolant channels, ASME Paper 96-TA-6 (1996).

[4] A. Murata, S. Mochizuki, T. Takahashi, Local heat transfer measurements of an orthogonally rotating square duct with angled rib turbulators, Int. J. Heat Mass Transfer 42 (1999) 3047–3056.

[5] P.R. Chandra, J.C. Han, S.C. Lau, Effect of rib angle on local heat/mass transfer distribution in a two-pass rib-roughened channel, Trans. ASME, J. Heat Transfer 110 (1988) 233–241.

[6] M. Hirota, H. Fujita, H. Yokosawa, T. Nakayama, T. Tanaka, Developing heat/mass transfer in low-aspect-ratio rectangular channels with ribbed walls, in: Heat Transfer 1998, Proceedings of 11th International Heat Transfer Conference, Taylor & Francis, vol. 5, 1998, pp. 363–368.

[7] G. Rau, M. Cakan, D. Moeller, T. Arts, The effect of periodic ribs on the local aerodynamic and heat transfer performance of a straight cooling channel, ASME Paper 96-GT-541 (1996).

[8] J.W. Baughn, X. Yan, Local heat transfer measurements in square ducts with transverse ribs, Enhanced Heat Transfer ASME HTD-Vol.202 (1992) 1–7.

[9] S.V. Ekkad, J.C. Han, Detailed heat transfer distributions in two-pass square channels with rib turbulators, Int. J. Heat Mass Transfer 40–11 (1997) 2525–2537.

[10] C. Prakash, R. Zerkle, Prediction of turbulent flow and heat transfer in a ribbed rectangular duct with and without rotation, Trans. ASME, J. Turbomachinery 117 (1995) 255–264.

[11] M.A. Stephens, T.I-P. Shih, K.C. Civinskas, Effects of inclined rounded ribs on flow and heat transfer in a square duct, AIAA Paper 95–2115 (1995).

[12] B. Banhoff, U. Tomm, B.V. Johnson, Heat transfer predictions for U-shaped coolant channels with skewed ribs and with smooth walls, ASME Paper 96-TA-7 (1996).

[13] B.E. Launder, D.P. Tselepidakis, B.A. Younis, A second-moment closure study of rotating channel flow, J. Fluid Mech. 183 (1987) 63–75.

[14] A. Huser, S. Biringen, Direct numerical simulation of turbulent flow in a square duct, J. Fluid Mech. 257 (1993) 65–95.

[15] S. Gavrilakis, Numerical simulation of low Reynolds number turbulent flow through a straight square duct, J. Fluid Mech. 244 (1992) 101–129.

[16] R.K. Madabhushi, S.P. Vanka, Large eddy simulation of turbulence-driven secondary flow in a square duct, Phys. Fluids A3-11 (1991) 2734–2745.

[17] T. Kajishima, Y. Miyake, T. Nishimoto, Large eddy simulation of turbulent flow in a square duct, Trans. JSME (B) 57–540 (1991) 2530–2537 (in Japanese).

[18] A. Murata, S. Mochizuki, Large eddy simulation with a dynamic subgrid-scale model of turbulent heat transfer in an orthogonally rotating smooth square duct, Int. J. Transport Phenomena, MS#99Nh/156, in press.

[19] A. Murata, S. Mochizuki, Effect of cross-sectional aspect ratio on turbulent heat transfer in an orthogonally rotating rectangular smooth duct, Int. J. Heat Mass Transfer 42 (1999) 3803–3814.

[20] A. Murata, S. Mochizuki, Large eddy simulation applied to internal forced-convection cooling of gas-turbine blades, in: Heat Transfer 1998, Proceedings of 11th International Heat Transfer Conference, Taylor & Francis, vol. 6, 1998, pp. 565–570.

[21] A. Murata, S. Mochizuki, Large eddy simulation with a dynamic subgrid-scale model of turbulent heat transfer in an orthogonally rotating rectangular duct with transverse rib turbulators, Int. J. Heat Mass Transfer 43 (2000) 1243–1259.

[22] M.E. Taslim, S.D. Spring, Effect of turbulator profile and spacing on heat transfer and friction in a channel, J. Thermophys. Heat Transfer 8–3 (1994) 555–562.

[23] G.J. Korotky, M.E. Taslim, Rib heat transfer coefficient measurements, in a rib-roughened square passage, ASME Paper 96-GT-356 (1996).

[24] J.C. Han, J.S. Park, C.K. Lei, Heat transfer enhancement in channels with turbulence promoters, Trans. ASME, J. Eng. Gas Turbines and Power 107 (1985) 628–635.

[25] S.V. Patankar, C.H. Liu, E.M. Sparrow, Fully developed flow and heat transfer in ducts having streamwise-periodic variations of cross-sectional area, Trans. ASME, J. Heat Transfer 99 (1977) 180–186.

[26] T. Kajishima, T. Ohta, K. Okazaki, Y. Miyake, High-order finite-difference method for incompressible flows using collocated grid system, JSME Int. J., Series B 41–4 (1998) 830–839.

[27] M. Germano, U. Piomelli, P. Moin, W.H. Cabot, A dynamic subgrid-scale eddy viscosity model, Phys. Fluids A3-7 (1991) 1760–1765.

[28] D.K. Lilly, A proposed modification of the Germano subgrid-scale closure method, Phys. Fluids A4-3 (1992) 633–635.

[29] C. Meneveau, T.S. Lund, W.H. Cabot, A Lagrangian dynamic subgrid-scale model of turbulence, J. Fluid Mech. 319 (1996) 353–385.

[30] P. Moin, K. Squires, W. Cabot, S. Lee, A dynamic subgrid-scale model for compressible turbulence and scalar transport, Phys. Fluids A3-11 (1991) 2746–2757.

[31] F.H. Harlow, J.E. Welch, Numerical calculation of time-dependent viscous incompressible flow of fluid with free surface, Phys. Fluids 8–12 (1965) 2182–2189.
[32] J. Kim, P. Moin, Application of a fractional-step method to incompressible Navier–Stokes equations, J. Comp. Phys. 59 (1985) 308–323.
[33] Y. Zang, R.L. Street, J.R. Koseff, A non-staggered grid, fractional step method for time-dependent incompressible Navier–Stokes equations in curvilinear coordinates, J. Comp. Phys. 114 (1994) 18–33.
[34] H. Yokosawa, H. Fujita, M. Hirota, S. Iwata, Measurement of turbulent flow in a square duct with roughened walls on two opposite sides, Int. J. Heat Fluid Flow 10–2 (1989) 125–130.
[35] W.M. Kays, M.E. Crawford, Convective Heat and Mass Transfer, third ed., McGraw-Hill, New York, 1993, pp. 116, 316.
[36] B.F. Armaly, F. Durst, J.C.F. Pereira, B. Schonung, Experimental and theoretical investigation of backward-facing step flow, J. Fluid Mech. 127 (1983) 473–496.